

Design and operation of APEX-LD: a compact levitated dipole for the confinement of electron–positron pair plasmas

A. Card,^{1, 2, a)} M.R. Stoneking,³ A. Deller,^{1, 4} and E.V. Stenson¹

¹⁾Max Planck Institute for Plasma Physics, 85748 Garching, Germany

²⁾Technical University of Munich, 80333 Munich, Germany

³⁾Lawrence University, Appleton, Wisconsin, 54911 USA

⁴⁾University of California San Diego, La Jolla, California, 92093 USA

(Dated: 11 November 2025)

The objective of the APEX (A Positron–Electron eXperiment) project is to magnetically confine and study electron–positron pair plasmas. For this purpose, a levitated dipole trap (APEX-LD) has been constructed. The magnetically levitated, compact (7.5-cm radius), closed-loop, high-temperature superconducting (HTS) floating (F-)coil consists exclusively of a No-Insulation (NI) Rare-earth Barium Copper Oxide (ReBCO) winding pack, solder-potted in a gold-plated-copper case. A resealable in-vacuum cryostat facilitates cooling (via helium gas) and inductive charging of the F-coil. The 70-minute preparation cycle reliably generates persistent currents of ~ 60 kA-turns and an axial magnetic flux density of $B_0 \approx 0.5$ T. We demonstrate levitation times in excess of three hours with a vertical stability of $\sigma_z < 20$ μm . Despite being subjected to routine quenches (and occasional mechanical shocks), the F-coil has proven remarkably robust. We present the results of preliminary experiments with electrons, and outline the next steps for injecting positron bunches into the device.

I. INTRODUCTION

Interest in electron–positron pair plasmas dates back nearly half a century.¹ The mass symmetry of pair plasmas is predicted to give rise to unique wave dynamics and notable stability compared to magnetized electron–ion plasmas.^{2,3} Moreover, there is evidence for naturally occurring electron–positron plasmas in the vicinity of extreme astrophysical objects.^{4–6} Recent efforts to produce electron–positron plasmas in the laboratory, using high-energy particle beams⁷ or intense lasers,⁸ have yielded dense, quasineutral distributions of unmagnetized, relativistic pairs. Targeting a different parameter regime, the APEX (A Positron–Electron eXperiment) project⁹ aims to create and confine low-temperature distributions of electrons and positrons and to investigate whether magnetized pair plasmas are as quiescent as predicted.¹⁰

The first challenge to producing an electron–positron plasma is the limited availability of antimatter. Our target density (n_e) and temperature ($k_B T$) regimes are based on those that have already been achieved with pure-positron (non-neutral) plasmas in linear traps ($n_e \sim 10^{12} \text{ m}^{-3}$; $k_B T \sim 1 \text{ eV}$).¹¹ The number of positrons required to produce a plasma scales with the device size, making smaller devices preferable, subject to limitations imposed by engineering, material, and experimental constraints. The reactor-based NEPOMUC (Neutron-induced Positron source MUNiCh) facility¹² is capable of delivering 5×10^7 remoderated (i.e., low-energy, high-brightness) positrons per second.¹³ It is conceivable, therefore, that $\sim 10^{10}$ positrons can be accumulated in a reasonable amount of time, sufficient for a confinement volume of $V \sim 10$ liters. Our target parameters correspond to a Debye length (λ_D , charge-screening length) of ~ 1 cm. As this is considerably shorter than the dimensions

of the confinement volume ($V^{1/3} \sim 22$ cm), collective plasma effects are expected to influence the particle behavior.¹⁴

The APEX levitated dipole (APEX-LD) has been designed to magnetically confine electron–positron pair plasmas.¹⁰ The magnetic field of the confinement volume is generated by current flowing in a superconducting coil that is magnetically levitated in vacuum. There are several engineering challenges associated with building a levitated dipole. The floating coil (F-coil) must be cooled to cryogenic temperatures and a persistent current must be generated in the closed loop of the superconductor. The F-coil must then be launched and stabilized, which can be accomplished using a concentric lifting coil (L-coil) to balance gravity. Earnshaw’s theorem states that there is no stable equilibrium in this configuration,¹⁵ thus the position of the F-coil must be continuously monitored and actively stabilized (e.g., by modulating the supply current of the L-coil).

Superconducting F-coils were first used for plasma studies in the levitated variants of the early “internal ring” devices, such as the Floating Multipole (FM-1) at PPPL. FM-1 explored toroidal field configurations such as the spherator, where the poloidal component of the field was supplied by a levitated coil.¹⁶ Inspired by the Voyager 2 discovery of high- β plasma in the Jovian magnetosphere¹⁷ (where β is the ratio of plasma / magnetic pressures), Hasegawa proposed that a levitated dipole could be employed in a fusion reactor.^{18,19} The Levitated Dipole Experiment (LDX) at MIT²⁰ and the Ring Trap devices (Mini-RT and RT-1) at the University of Tokyo^{21,22} were built to investigate this concept. Experiments with these devices have demonstrated turbulence-driven inward transport of confined quasineutral electron–ion plasmas²³ and local plasma β exceeding unity.²⁴ Self-organization of a pure-electron plasma into a magnetospheric vortex with a centrally peaked density profile was also observed in RT-1.²⁵

In addition to the superconducting winding pack, the F-coil assemblies of previous devices have typically included an on-

^{a)}Electronic mail: alexander.card@ipp.mpg.de

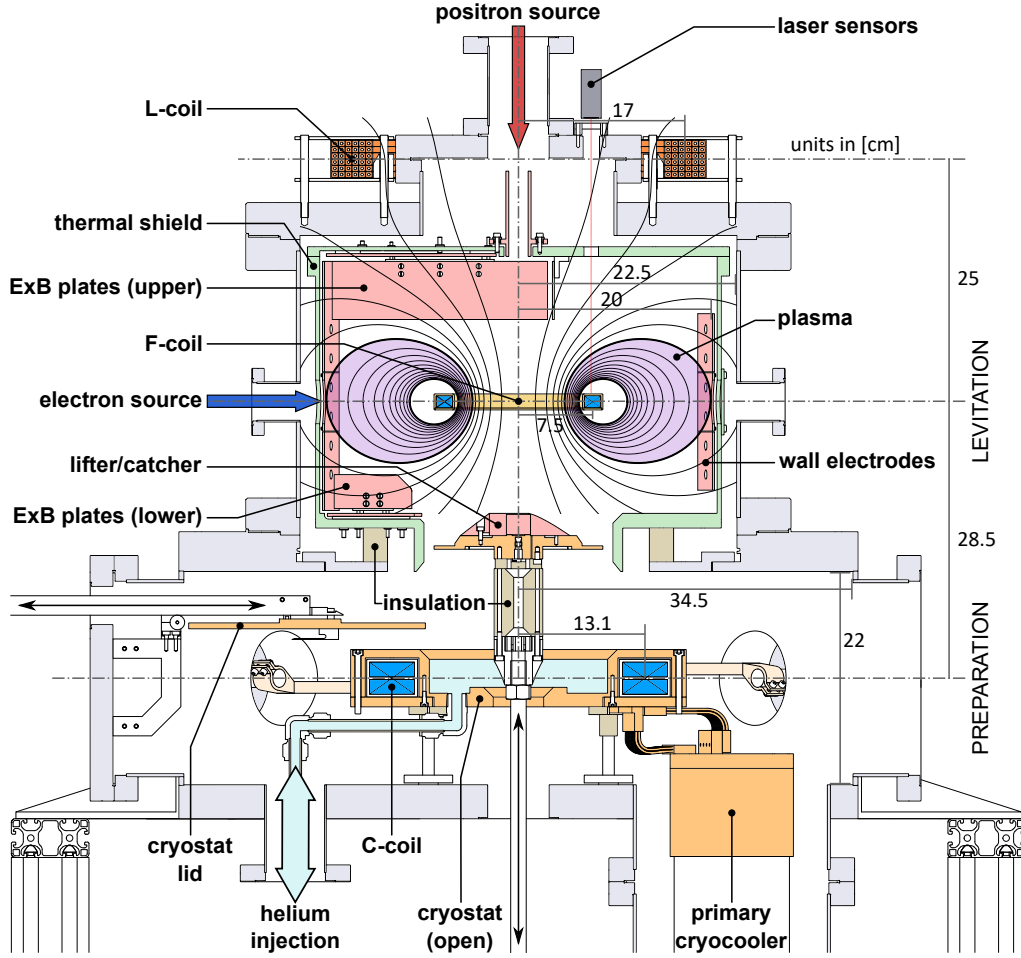


FIG. 1. Schematic of APEX-LD during the levitation phase of operation. The upper levitation region hosts the F-coil (which produces the purple confinement region), L-coil, laser displacement sensors, thermal shield (green), and particle injection electrodes (pink). The lower preparation region hosts the cryostat (open, lid retracted), C-coil, primary cryocooler, horizontal and vertical translators (arrows indicate motion), and helium injection tubing. The lifter/catcher platform transports the F-coil between the two regions.

board cryostat with multi-layer insulation and demountable transfer lines for liquid or gaseous helium.^{26–30} Energization of a persistent current was achieved either with a direct current (via detachable leads connected in parallel with a persistent current switch^{26,31,32}) or inductively using an additional charging coil (C-coil).³³ Flux pumps are currently being pioneered as an alternative approach by OpenStar Technologies in the private sector.³⁴ During levitation, the feedback-stabilized position of the F-coil was measured optically, either through occultation of a light source (using focused lamps³⁵ or lasers³⁶) or with laser displacement sensors.^{37,38}

Our application constraints led us to make several design choices that distinguish APEX-LD from similar devices.³⁹ The F-coil consists of a superconducting winding pack in a thin copper case to maximize the region of high magnetic field for plasma confinement. Contactless inductive charging within a resealable cooling enclosure allows us to eschew demountable connections. The correspondingly minimalist F-coil design takes advantage of recent developments with No-Insulation (NI) Rare-earth Barium Copper Oxide (ReBCO)

high-temperature superconducting (HTS) materials, and fully soldered manufacturing techniques, to realize long levitation times and passive quench protection. We stabilize levitation of the F-coil to a precision of $\sigma_z \sim 20 \mu\text{m}$ using feedback provided by a Field-Programmable Gate Array (FPGA) and real-time controller.⁴⁰

This paper is organized as follows. Section II details the design of the system, with focus placed on the HTS coils (Sec. II A), integrated cooling and charging station (Sec. II B), and feedback-stabilized levitation system (Sec. II C). Section III describes the operation of APEX-LD, including the F-coil preparation (Sec. III A) and levitation (Sec. III B) phases, as well as a subsection on quenching and overall coil robustness (Sec. III C). Section IV presents preliminary experiments with electrons that demonstrate the confinement capabilities of the device. In the final Section V, we provide a discussion of future developments for APEX-LD.

TABLE I. APEX-LD parameters

F-coil	
Conductor material	NI GdBCO
Operating $T \mid T_c$	20 – 75 K \mid 92 K
Average radius r_F	7.5 cm
Winding pack $w_F \times h_F$	1.6×1.3 cm
Copper case $w_c \times h_c$	2.1×1.7 cm
Mass m_F	1.34 kg
Self-inductance L_F	6.2 mH
Resistance (@ 20 K) R_F	72 n Ω
Decay time constant $\tau = L_F / R_F$	24.1 h
Persistent current $I_F \times N_F$	$398 \text{ A} \times 150 \text{ t} = 59.7 \text{ kA-t}$
Flux Φ_F	16.5 mWb
Flux density $B_{max} \mid \text{axial } B_0$	1.2 T \mid 0.5 T
Stored energy U_F	493 J
C-coil	
Conductor material	GdBCO
Operating $T \mid T_c$	25 K \mid 92 K
Average radius r_C	13.1 cm
Winding pack $w_C \times h_C$	4.6×3.3 cm
Vertical position* z_C	–28.5 cm
Self-inductance L_C	56 mH
Current $I_C \times N_C$	$370 \text{ A} \times 410 \text{ t} = 151.7 \text{ kA-t}$
Flux Φ_C	50.3 mWb
Stored energy U_C	3.4 kJ
L-coil	
Conductor material	Copper
Operating T	290 K
Average radius r_L	17 cm
Cross section $w_L \times h_L$	4.4×4.0 cm
Vertical position* z_L	25 cm
Current $I_L \times N_L$	$80 \text{ A} \times 36 \text{ t} = 2.9 \text{ kA-t}$
System	
Cooldown (300 K \rightarrow 20 K)	5.5 h
Preparation	
Initial cycle time	70 min
Subsequent cycles	45 min
Levitation	
Time	3.25 h
Stability σ_z	18 μm
Plasma confinement volume	10 liters

*relative to levitated F-coil

II. DESIGN

A schematic overview of APEX-LD is provided in Fig. 1. The ultra-high vacuum (UHV) chamber comprises two distinct regions. The lower preparation region contains a re-sealable cryostat (unsealed/open in Fig. 1), which cools the F-coil and encloses the C-coil used to induce a persistent current in its HTS windings. The upper levitation region contains the thermal shield, injection electrodes, and plasma diagnostics. The vertically translating lifter/catcher platform provides transport between the two regions. Fig. 1 depicts APEX-LD during levitation. At the end of a levitation cycle, the F-coil is caught by the platform and returned to the preparation region.

The plasma confinement volume is limited on the inboard

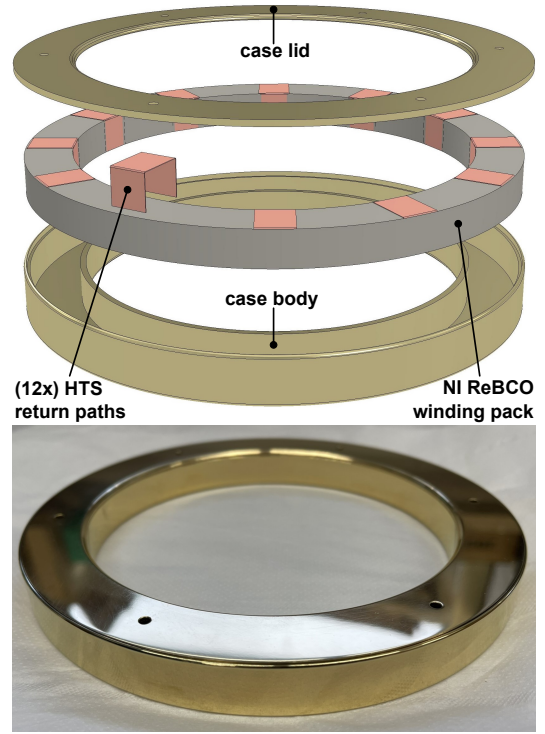


FIG. 2. (top) Exploded schematic of the F-coil. The NI ReBCO HTS winding pack is a single-pancake coil of 150 turns closed by twelve radial bands connected in parallel. The fully soldered winding pack is soldered into a gold-plated copper case. (bottom) A photograph of the manufactured F-coil.

side by the F-coil and on the outboard side by the wall electrodes at radius $r = 20$ cm. The toroid formed by the uninterrupted field lines of the levitating coil has a volume of 10 liters. The electrodes and thermal shield have not yet been installed and are part of a planned upgrade that will be discussed in Sec. V. Table I presents key physical and operational parameters for APEX-LD.

A. High-temperature superconducting coils

APEX-LD features two HTS coils (F-coil and C-coil) that were engineered in close collaboration with THEVA GmbH. While the two coils differ in design (e.g., single versus double pancake), they are both manufactured using ReBCO HTS tape produced by THEVA. The specific HTS compound is Gadolinium Barium Copper Oxide (GdBCO), which has a superconducting transition at $T_c \approx 92$ K.⁴¹ The tape is composed of a thin superconductor layer ($\sim 5 \mu\text{m}$) deposited onto a magnesium oxide-coated Hastelloy substrate, which is then silver plated.⁴² Copper electroplating brings the thickness of the non-insulated tape utilized by the F-coil to 120 μm . The polyimide-insulated tape used for the C-coil also includes an extra layer of copper laminate and has an overall thickness of 220 μm . Both coils were constructed using 12-mm-wide tape (minimum normal bending radius of 3 cm).

Figure 2 presents an exploded view of the F-coil design and

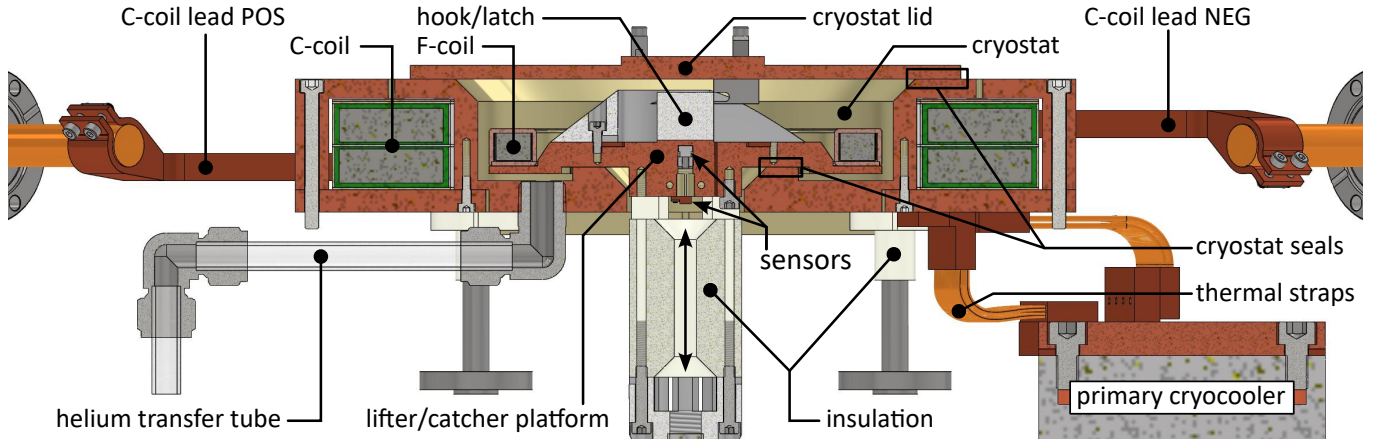


FIG. 3. Cross section of the cryostat CAD model, presented in the closed (sealed) configuration for F-coil preparation. Note the coplanar, concentric alignment of the F-coil relative to the C-coil for good inductive coupling.

a photograph of the manufactured coil. It is a closed coil with no external leads nor persistent current switch. The coil must be inductively energized and resilient to routine quenches. At the time of manufacture, only 12-mm-wide ReBCO tape was accessible, so a single-pancake design was chosen. The winding pack consists of 150 turns with an average radius of 7.5 cm. Twelve U-shaped strips of ReBCO connect the inner and outer turns, providing a low-resistance parallelized return path for persistent current. The F-coil has a mass of 1.34 kg and a square cross-sectional area of 3.6 cm^2 .

The F-coil NI winding pack is stabilized with tin-silver-copper solder (Sn96.5–Ag3.0–Cu0.5) and potted with indium-silver solder (In97–Ag3) inside a thin, gold-plated, oxygen-free copper (Cu-OF) case. The fully soldered coil is mechanically, thermally, and electrically contiguous. The low-emissivity case shields the winding pack from thermal radiation. Its thin profile minimizes shadowing of the poloidal magnetic field lines closest to the coil.

The C-coil is used to inductively charge the F-coil. It comprises 410 turns of 12-mm-wide, turn-to-turn insulated HTS tape, in a double-pancake configuration with the open ends soldered to copper electrodes. The average radius of the C-coil is 13.1 cm, with winding pack dimensions of 46 mm (horizontal) by 33 mm (vertical). It is stabilized with a low out-gassing epoxy resin and sealed in the gold-plated Cu-OF enclosure of the cryostat (Sec. II B).

B. Integrated cooling and charging station

The F-coil is cooled and charged in a resealable cryostat located in the lower preparation chamber. Figure 1 presents the cryostat in the open (unsealed) configuration employed during levitation. The closed (sealed) configuration is presented in Fig. 3. At the center of the cryostat is a cavity into which the F-coil is retracted. The coplanar, concentric alignment between the two coils maximizes inductive coupling. A horizontal translator transfers the cryostat lid to the lifting platform using two sets of hooks and latches. Fully retracting the

lifter engages two annular metal-to-metal seals, isolating the cavity volume from the rest of the vacuum chamber. The gold-plated-copper seals also provide good thermal contact, which ensures the lid and lifter rapidly thermalize with the cryostat body.

The primary cryocooler (Cryomech AL630) is connected to the cryostat with four flexible Cu-OF thermal straps, which provide vibration isolation and a thermal conductance of 6.7 W/K at 20 K. Thermal conductivity between the F-coil and cryostat is established through i) direct contact with the lifter, ii) blackbody radiation, and iii) an exchange gas (helium), which is transferred to and vented from the cryostat via a plastic (PFA) tube. With the cryostat lid sealed, helium can be introduced using a stepper-motor-controlled leak valve. In combination with a turbomolecular pump (Leybold TURBO-VAC MAG W 1300 iP), the metal seals allow the cryostat to be pressurized to $\sim 1 \text{ mbar}$ with helium while maintaining a pressure of $< 1 \times 10^{-4} \text{ mbar}$ in the vacuum system. The cryostat is supported on four stainless steel legs that are thermally insulated from the vacuum chamber by TECASINT 2011 stand-offs (see Fig. 3). From room temperature, the station cools to its base temperature of 20 K in 5.5 h, with the F-coil trailing by 1 h (without an exchange gas).

Magnetic field strength is measured using a Hall sensor embedded in the lifter assembly (centered and coplanar with the two HTS coils). The lifter platform is thermally and electrically isolated from the vertical translator using a TECASINT 2011 insulation standoff. This allows the lifter to serve as a plasma diagnostic (capacitive probe or charge collector), or it can be biased to assist with charged particle injection.

The C-coil enclosure is cooled by the primary cryocooler. Two pieces of single-crystal sapphire (Al_2O_3) ensure good thermal contact between the enclosure and C-coil electrodes without shorting the latter to ground. The cryogenic surfaces act as a cryopump that adsorbs impurities outgassing from the stabilizing epoxy. Current is supplied to the C-coil through two actively cooled leads (POS and NEG in Fig. 3). Each lead consists of a 270-mm Cu-OF busbar that thermally connects a room-temperature vacuum feedthrough to the sec-

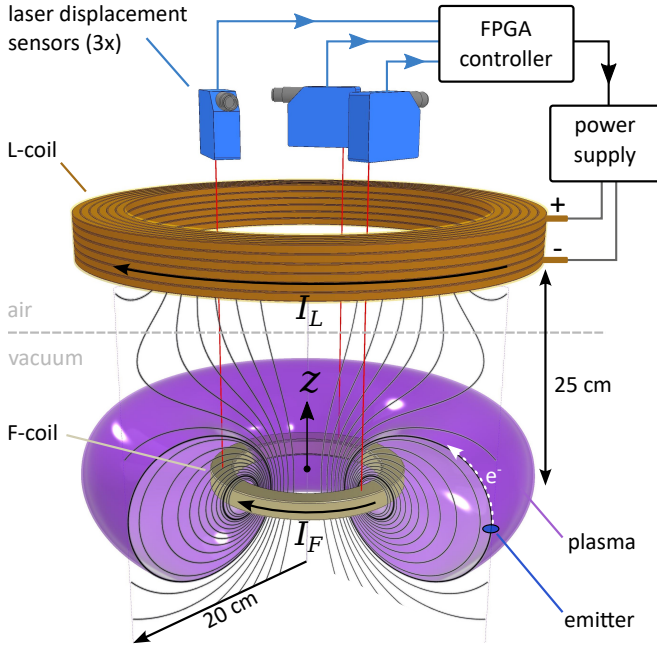


FIG. 4. The feedback-stabilized levitation system. The larger diameter L-coil, located above, naturally stabilizes the slide and tilt motions of the F-coil. The feedback loop stabilizes the vertical motion (\hat{z}). An electron emitter can be inserted onto outboard field lines to inject electrons into the confinement volume.

ondary cryocooler (Leybold COOLPOWER 250 MD), followed by two parallel strips of 12-mm-wide NI GbBCO HTS tape that connect to the C-coil electrodes. The 160-mm-long HTS bridges minimize the ohmic and conductive heat load to the C-coil (and provides vibration isolation). Similarly, the cross-sectional area of the Cu-OF busbars (12×3 mm) is a compromise of thermal and electrical conductivity that minimizes the heat load to the secondary cooler during C-coil energization. On one end, the HTS strips are soldered to each busbar with a ~ 70 -mm overlap and the connections are clamped to the secondary cryocooler through sapphire insulators, reaching thermal equilibrium at 31 K (32 K when the C-coil is energized). On the opposite end, each HTS strip is soldered with a ~ 20 -mm overlap to a Cu-OF adapter that clamps to the C-coil electrode. The C-coil power supply (Cryogenic SMS450C 4Q T R/M) provides up to 400 A of current with built-in quench protection. The maximum current that we can continuously supply to the C-coil is limited to ~ 370 A (152 kA-t) by the HTS bridges. When the C-coil is energized, the lead assemblies contribute 4 W of heat to the C-coil and 50 W to the secondary cryocooler.

C. Feedback-stabilized levitation control

The energized F-coil is magnetically levitated using the L-coil located above the vacuum chamber. The axisymmetric coil geometry is configured to be inherently stable for five of the six degrees of freedom: slide (xy), tilt (pitch, roll), and azimuthal (yaw) rotation.⁴³ The vertical (z) position, how-

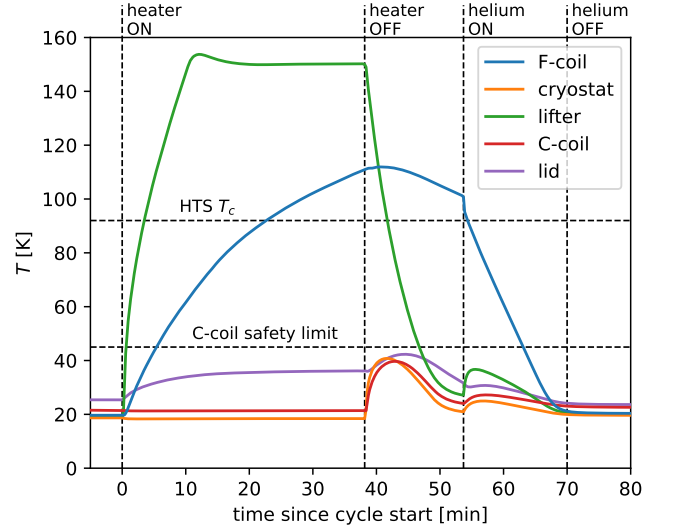


FIG. 5. Temperature of the cryostat and HTS coils during F-coil preparation. The F-coil is heated by the lifter above T_c and then rapidly re-cooled using helium gas. The C-coil is kept below 45 K so it can safely energized during the charging procedure.

ever, must be actively stabilized. Our stabilization system is based on digital PID feedback implemented by an FPGA-based controller.⁴⁰ The software was developed using a test levitation system and a neodymium permanent magnet.⁴³

The physical components of the levitation system are presented in Fig. 4. The F-coil is located inside the vacuum chamber, whereas the laser displacement sensors, FPGA-controller, L-coil, and its power supply (Regatron TopCon Quadro⁴⁴) are all located outside of the vacuum system. The L-coil is wound from square copper profile with a central channel for water cooling. The 6×6 turn winding pack has an average radius of 17 cm. The L-coil is positioned 25 cm above the levitation plane and can be continuously driven with up to 200 A of DC current.

The stabilization flow diagram is shown in Fig. 4. Three laser displacement sensors measure the vertical position of the F-coil. The FPGA controller digitizes the sensor signals, rejects any out-of-range values (e.g., due to sensor blinding), and then feeds the average into a PID algorithm. The digital PID output is then post-processed (e.g., range coercion) and converted to an analog output signal that manipulates the L-coil power supply current to correct displacements from the setpoint position. The magnetic field of the L-coil represents only a small (and axisymmetric) perturbation to the confinement field (2.9 kA-t in the L-coil versus 60 kA-t in the F-coil).

III. OPERATION

A. Preparation

The inductive charging procedure thermally cycles the F-coil above and below its critical temperature, $T_c \approx 92$ K while

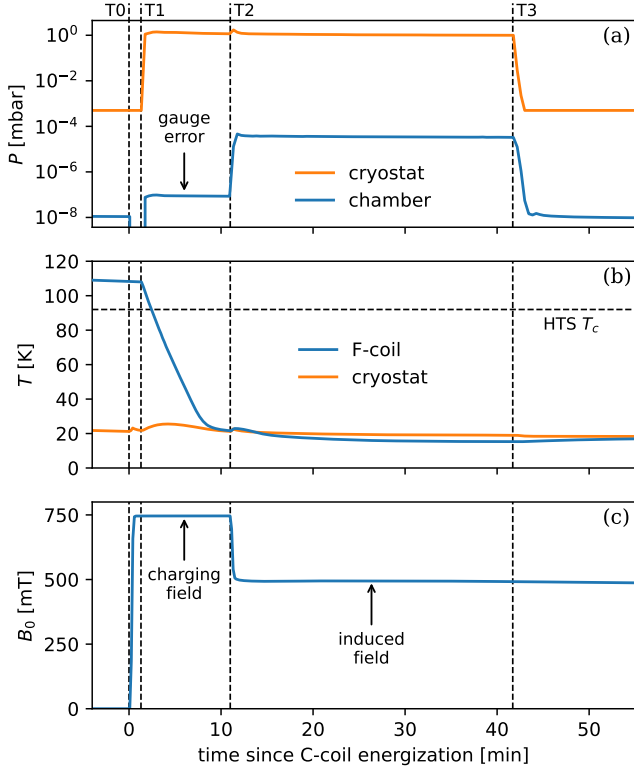


FIG. 6. (a) Pressure, (b) temperature, and (c) axial magnetic flux density during the first F-coil induction test. Prior to the start, the F-coil was warmed to a normally conducting state. At T_0 the C-coil is ramped on (750 mT). Helium is injected at T_1 to cool the F-coil below the superconducting transition. At T_2 the C-coil is ramped off, inducing a persistent current in the F-coil. Helium is vented at T_3 , and the preparation phase is complete.

keeping the C-coil below 45 K (the limit for safely energizing with 400 A). Measurements of the cryostat and F-coil temperatures during preparation are presented in Fig. 5. At $t = 0$, the lifter is raised by 1.5 mm to thermally disconnect it from the cryostat. The F-coil is then warmed above its superconducting transition using a resistive heater embedded in the lifter and a PID feedback controller (Lake Shore Cryotronics Model 336) with a 150-K setpoint. After 38 minutes, the F-coil has warmed to 110 K, at which point the heater is disengaged and the cryostat is resealed. At $t = 54$ minutes, the C-coil is turned on and the F-coil is re-cooled by helium gas, which is introduced into the cryostat via a stepper-motor-controlled leak valve connected to the transfer tube. This raises the pressure in the cryostat to ~ 1 mbar and establishes a strong thermal connection between the F-coil and cryostat. At $t = 70$ minutes, the F-coil has reached its base temperature and the helium is vented.

Figure 6 presents the pressure P , temperature T , and axial magnetic flux density B_0 during the inductive charging procedure. At T_0 , the F-coil is not superconducting. The C-coil is ramped to 152 kA-t over 10 s, which generates a magnetic field of 750 mT at its center. The drop in the measured chamber pressure is caused by the stray magnetic field

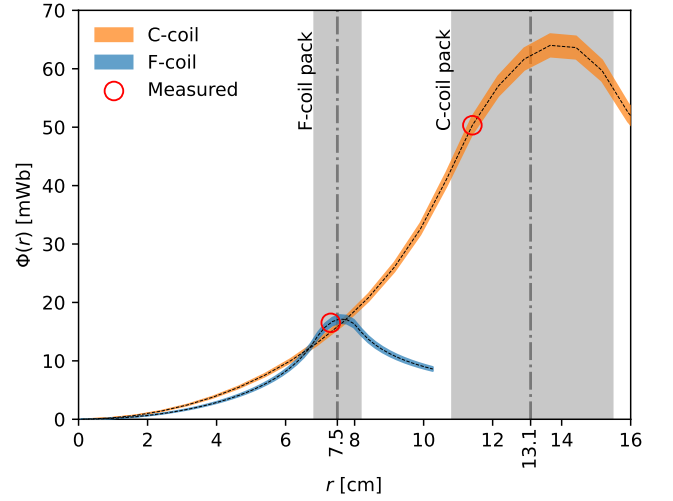


FIG. 7. Radially integrated flux as a function of r for the C-coil (with 152 kA-t) and the F-coil (with 60 kA-t) at $z = 0$. For each curve, the shaded extent along the ordinate represents the uncertainty. Intersection of measured flux values with the calculated curves are circled in red for each coil.

at the ion gauge. At T_1 , helium begins to cool the F-coil (i.e., $t = 54$ minutes in Fig. 5) and at T_2 it has reached its base temperature. This particular measurement was taken before the HTS winding pack was soldered into the copper case, resulting in a slightly faster cooldown than shown in Fig. 5. With the F-coil now superconducting, the C-coil can be ramped off, which induces a persistent current of $I_F \approx 400$ A in the F-coil (i.e., $N_F I_F = 60$ kA-t; $B_0 = 500$ mT). This indicates that the F-coil captures a sizable portion of the C-coil flux. Normally, the helium is vented immediately after charging the F-coil. However, for the measurement shown in Fig. 6, the pressure was maintained for 30 minutes for testing purposes. The large pressure differential between the inside and outside of the cryostat ($P_{\text{cryostat}} \approx 10^4 \times P_{\text{chamber}}$) allows the F-coil to be rapidly cooled without warming the cryostat / cooling the vacuum vessel.

The total magnetic flux Φ , through a surface S , is given by the surface integral of the normal component of the magnetic flux density \mathbf{B} . Assuming rotational symmetry about the z -axis and a circular surface with radius r at a height $z = 0$, this reduces to

$$\Phi(r) = \iint_{S(r)} \mathbf{B}(r, z) \cdot d\mathbf{S} = \int_0^r B_z(\rho, 0) 2\pi \rho d\rho. \quad (1)$$

Applying the Biot-Savart law to an infinitesimally thin, current-carrying loop of radius a provides an analytical expression for the z component of the off-axis magnetic field $B_z(\rho, z)$, in the plane of the loop ($z = 0$),

$$B_z(\rho, 0) = \frac{\mu_0 I}{2\pi(a + \rho)} \left[K(k^2) + \frac{(a^2 - \rho^2)}{(a - \rho)^2} E(k^2) \right], \quad (2)$$

where K and E are complete elliptical integrals of the first and

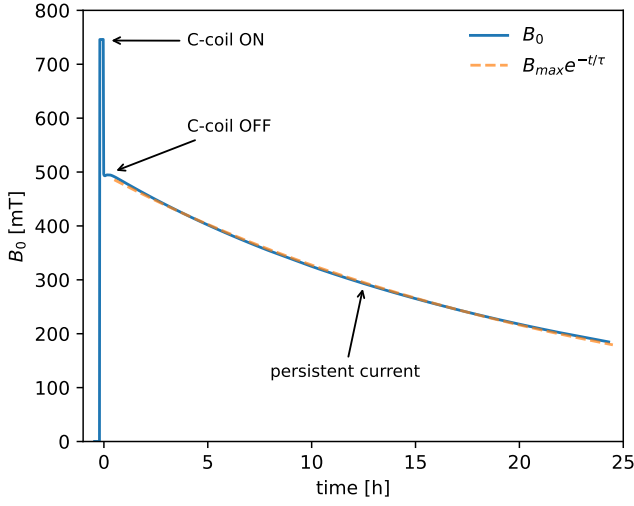


FIG. 8. Slow decay of the axial magnetic field B_0 (measured at the center of the F-coil) when the charged F-coil is maintained at $T = 20$ K (i.e., the continuation of Fig. 6c). The measured decay time is $\tau = 24.1$ h.

second kind,⁴⁵ and

$$k^2 = \frac{4a\rho}{(a+\rho)^2}. \quad (3)$$

The total flux enclosed by a coil with a finite winding pack can be determined from the superposition of the flux generated by an offset stack of concentric current loops.

Figure 7 shows the calculated enclosed flux as a function of r (in the symmetry plane of the coils) for the fully energized C-coil, $\Phi_C(r)$. Also shown is the equivalent calculation for the inductively charged F-coil, $\Phi_F(r)$. The radial extent of each winding pack is shaded gray. The flux of each coil was independently estimated by integrating the measured back electromotive force (EMF) as the C-coil was ramped on (F-coil not superconducting) and off (F-coil superconducting). The intersection of the measured values [$\Phi_F(r_F) = 16.5$ mWb; $\Phi_C(r_C) = 50.3$ mWb] and the calculated curves are circled in red. The two curves closely match at the location of the F-coil, $\Phi_F(r_F) \approx \Phi_C(r_F)$, which suggests that all of the geometrically available flux is captured.

To measure the internal resistance of the F-coil, we observe the L/R decay of its persistent current with the coil maintained at base temperature, as presented in Fig. 8. Fitting the exponential decay to $B_{\max}e^{-t/\tau}$ indicates a decay time of $\tau = 24.1$ h. The self-inductance of the F-coil is calculated from its geometry to be $L_F = N_F\Phi_F/I_F = 6.2 \pm 0.3$ mH. Therefore, the residual resistance of the solder joints at 20 K is estimated to be $R_F = 72 \pm 4$ n Ω .

B. Levitation

Upon completion of the preparation phase, the cryostat is opened using the two linear translators. The lifter/catcher platform, attached to the vertical translator, includes a latch that

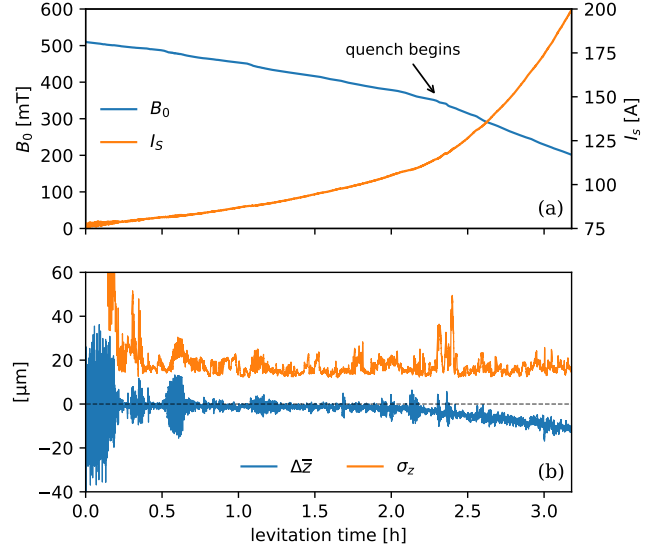


FIG. 9. An example of a full levitation cycle. (a) Axial magnetic flux density B_0 and L-coil supply current I_s required to maintain the F-coil setpoint position. (b) The average vertical displacement $\Delta\bar{z}$ and stability σ_z of the F-coil over a 10-s rolling window.

couples with cantilevered hooks on the underside of the cryostat lid (see Fig. 3). A horizontal translator arm, featuring a trident hook, enters from the side and engages with three latches on top of the lid. The horizontal arm decouples the lid from the vertical translator and then retracts it out of the way (see Fig. 1). With the cryostat opened, the lifting platform is clear to lift the F-coil into the launching position. At this point, the FPGA-based levitation controller and L-coil supply are switched on. As the L-coil lifts the F-coil, eddy currents are induced in the copper lifting platform. This causes the launching coil to tilt, resulting in temporary failures of the displacement sensors. The associated error signals are automatically handled by the controller software, allowing it to continue the launch and then stabilize the position of the F-coil.⁴⁰

Figure 9 presents an example levitation cycle. Figure 9a shows the axial flux density B_0 at the center of the F-coil (calculated from the lifter Hall sensor and laser position measurements) and manipulated L-coil supply current I_s (approximately equal to I_L) required to maintain the setpoint position z_F . Figure 9b shows the average vertical displacement $\Delta\bar{z}$ and standard deviation of the averaged laser sensor signal σ_z (i.e., the vertical stability), both taken over a 10-s rolling window (with an acquisition rate of 100 Hz). The total levitation time is 3.25 h, with a vertical stability of $\sigma_z = 18$ μm , calculated over the full cycle.⁴⁰

C. Quenching

The NI ReBCO construction of the APEX-LD F-coil has exceeded expectations in terms of robustness. In Fig. 9a, we see the point at which the quench begins. During levitation,

thermal radiation gradually warms the F-coil, which increases the resistance of the current path and increases the rate of decay. As the coil continues to warm, the critical current threshold also steadily decreases. This continues until the circulating current matches the critical current of the HTS tape, which provokes a notable increase in the decay rate. Since the current is not driven, any excess current is diverted through the resistive layers of copper and solder. This threshold quenching process dissipates the energy stored in the magnetic field very slowly, which allows the F-coil to continue levitating for an additional 50 minutes.

The magnetic field energy of the fully-charged F-coil is $U_F \approx 500$ J. At the onset of the quench, the current in the F-coil has resistively decayed, resulting in a reduction of B_0 to $0.7B_{max}$ (350 mT). During the following 50-min quenching period B_0 further reduces to $0.4B_{max}$ (200 mT). Assuming the self-inductance (L) is constant, and

$$U = \frac{1}{2}LI^2 \Rightarrow U \propto B_0^2, \quad (4)$$

the reduction of B_0 by $\Delta B_{quench} = 0.3B_{max}$ results in a conversion of $\Delta U_{quench} = 0.09U_{max} \approx 36$ J of magnetic energy into heat energy (Q). Using the mass (m) of the F-coil, and specific heat capacity (C) of Cu-OF copper ($RRR = 100$; 60 K), we calculate a F-coil temperature rise using

$$\Delta T = \frac{Q}{mC}. \quad (5)$$

Inserting values into Eq. 5 predicts an increase of $\Delta T \approx 0.7$ K over the 50-min quench. This excess heat is easily absorbed by the solid mass of the F-coil, and corroborates the observation that when a thermal sensor was installed during commissioning, we did not see a measurable change in the F-coil temperature during the quench.

APEX-LD has performed over 30 levitation cycles, all of which ended in an F-coil quench. Furthermore, the coil has endured a mechanical impact against the ceiling of the vacuum chamber at an estimated velocity of 5 m/s. Nevertheless, we have been unable to measure any degradation in performance of the fully soldered HTS coil.

IV. ELECTRON EXPERIMENTS

A. Field line visualization

APEX-LD employs a lanthanum hexaboride (LaB_6) thermionic electron emitter mounted to a linear manipulator in the midplane of the levitation chamber (see Fig. 4). The crystal emission plane is oriented to emit electrons vertically, i.e., parallel to the outer magnetic field lines of the F-coil.⁴⁶ By injecting helium gas into the UHV chamber, the continuous electron beam can be imaged, a photograph of which is presented in Fig. 10. Visualization is typically performed with an emitter heating current of 1.2 A, an acceleration potential of -100 V, and a helium pressure in the range of 10^{-5} to 10^{-3} mbar.

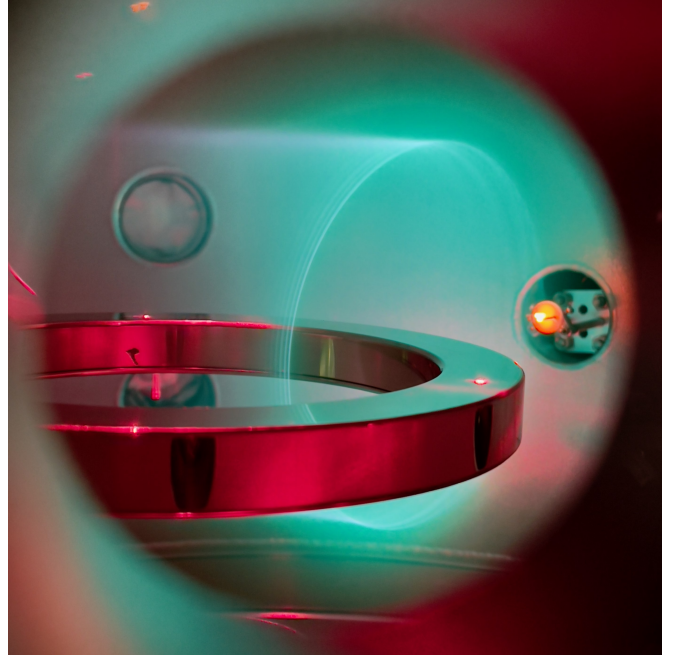


FIG. 10. Photograph of the levitating F-coil. A LaB_6 cathode injects electrons from the edge of the confinement volume. The electrons follow the poloidal field lines of the coil and drift toroidally. The beam path is visualized using dilute helium gas ($P \sim 10^{-3}$ mbar). Reflections of the red laser displacement sensors are also visible. The viewing angle is restricted by the tube of the DN40CF flange.

The 100-eV electrons excite and ionize the helium atoms. The resultant radiative decay produces a faint glow that illuminates the electron beam path. In addition to the gyromotion around the magnetic field (not discernible in Fig. 10), the electrons stream poloidally along the field lines and through the center of the F-coil, and they drift toroidally in the counter-clockwise direction (viewed from above) due to field curvature and grad-B drifts.⁴⁷ The gyromotion occurs on the GHz scale, the poloidal motion on the MHz scale, and the toroidal motion on the kHz scale. The helical path of the poloidal and toroidal motion is clearly visible in Fig. 10. The magnetic focusing of the beam as it enters the high-field region in the center of the F-coil is also visible. After ~ 5 poloidal transits, collisions and shear in the electron drift velocities causes the beam to smear into a diffuse toroidal surface.

B. Pure-electron plasmas

We have performed preliminary experiments with pure-electron plasmas that verify the trapping capabilities of APEX-LD. Under UHV conditions, the LaB_6 emitter on the edge of the confinement volume is switched from ground to a negative bias to produce a short pulse of electrons (filling time 100 μs to 1 s; injection energy 50 to 150 eV). The emitted electrons follow the drift orbits shown in Fig. 10. A small fraction diffuses radially inward and establishes a non-neutral plasma with a large space-charge potential.⁴⁶

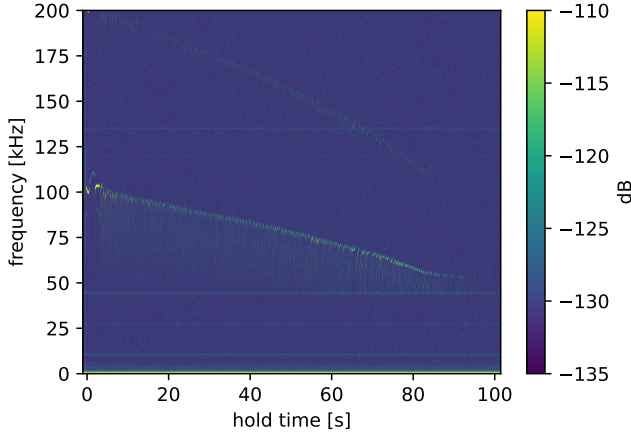


FIG. 11. An example FFT spectrogram of wall-probe measurements with a trapped pure-electron plasma. The slowly decaying toroidal mode ($f_0 \approx 100$ kHz) demonstrates long-term plasma confinement.

The dynamics of the trapped electrons are observed during the hold period, which commences after the fill is terminated by grounding the emitter bias. Plasma fluctuations are detected using capacitive wall probes installed on the equator of the confinement volume. Time-resolved Fourier spectra of the induced image currents ubiquitously exhibit a distinct mode that is consistent with a diocotron mode with a toroidal mode number $\ell = 1$.⁴⁶ The mode frequency f_0 is typically between 100 and 400 kHz, with harmonics often visible into the MHz range (these arise as a consequence of the small size of the probes relative to the plasma).⁴⁸

Low-order diocotron modes can be remarkably stable.⁴⁹ In APEX-LD, the mode commonly persists for $t_{\text{hold}} \approx 10$ s. For certain injection parameters, however, we have observed plasma oscillations throughout much longer hold times, as demonstrated in Fig. 11. For this measurement, the initially stable mode quickly evolves into a series of upwards chirps. The end frequency steadily droops from roughly 100 to 50 kHz, presumably due to the loss of electrons and the corresponding decrease in space-charge potential.⁴⁶ The mode is clearly visible for $t_{\text{hold}} \approx 90$ s, which illustrates the impressive confinement capabilities of levitating dipole traps. Even longer confinement times of pure-electron plasmas (> 300 s) have been reported by RT-1.^{25,50}

V. DISCUSSION AND FUTURE WORK

In this paper, we have presented the design and operation of APEX-LD, a new device which can repeatedly cool, inductively charge, and stably levitate a closed-loop superconducting coil under UHV conditions. Since the first charging and levitation trials in August 2023, we have performed field line visualization tests and demonstrated excellent confinement of pure-electron plasmas.⁴⁶ The success of these measurements, coupled with the robustness of the coil and reliability of our preparation procedures, provide us with confidence that this

novel device is well-suited for future experiments with pair plasmas.

The fully soldered construction of the NI ReBCO F-coil offers unique benefits in the application of a levitated dipole. Mechanically, the solder provides remarkable robustness. We have verified this through dozens of thermal and electrical cycles, each ending with a quench, without any apparent degradation in performance. The solder provides good thermal conductivity between the HTS windings and case, which helps to minimize the preparation time. From room temperature, the system cools to 20 K in 5.5 h, with the F-coil trailing by 1 h. From its base temperature, the F-coil can be prepared for levitation in 70 minutes (i.e., 35% of our levitation time of 195 minutes). After levitation, the warming phase of preparation can be significantly shortened, allowing for a recharging time of only 45 minutes. Accordingly, multiple cycles can be conducted per day.

The single-pancake F-coil design is a compromise necessitated by the availability of only 12-mm-wide HTS tape at the time of manufacture. Although the coil performs well (resistance at base temperature of 72 n Ω), the radial bands introduce asymmetries that we would rather avoid. In the near future, we plan to upgrade the F-coil to a double-pancake wound from a single piece of 6-mm-wide NI ReBCO tape. In addition to enhancing the toroidal symmetry of the magnetic field, we estimate the increased inductance and reduced resistance could extend our L/R decay time by an order of magnitude. Our levitation time is presently limited by exposure of the F-coil to room-temperature blackbody radiation. For this reason, an actively-cooled heat shield is under construction that will enclose over 95% of the surface area of the levitation region (see Fig. 1) and reduce the F-coil warming rate.

Confinement of a pair plasma in APEX-LD requires the injection of both positive and negative charge species; this is a challenge because the positrons arrive independently of electrons. One approach is to generate neutral, Rydberg positronium atoms, which can drift across field lines before undergoing ionization within the confinement volume.⁹ However, this method must contend with compounding inefficiencies.¹⁰ Another promising injection strategy is based on drifting bunches of positrons into an established electron plasma.⁵¹ Our experiments with electrons have enabled us to refine our techniques for the production and control of stable non-neutral electron plasmas in APEX-LD. Cold, dense pulses of positrons, supplied by linear traps,^{52,53} will arrive from above, along the center axis (see Fig. 1), and will be injected using an $\mathbf{E} \times \mathbf{B}$ drift technique.⁵⁴ This uses electrodes (incorporated into the heat shield design) to steer the charged particles from the open transport field lines into the closed confinement volume.⁵⁵

Figure 12 presents a trajectory calculation of $\mathbf{E} \times \mathbf{B}$ injection into APEX-LD. The particle enters through the top, passing first through a static, orthogonal electric field that produces an $\mathbf{E} \times \mathbf{B}$ drift towards the closed field lines. Biased upper and outer wall electrodes prevent the particle from colliding with the thermal shield. Simulations of positron distributions typical of linear traps suggest that high injection efficiencies are achievable. Lossless drift injection of positron bunches into a supported dipole trap was recently demon-

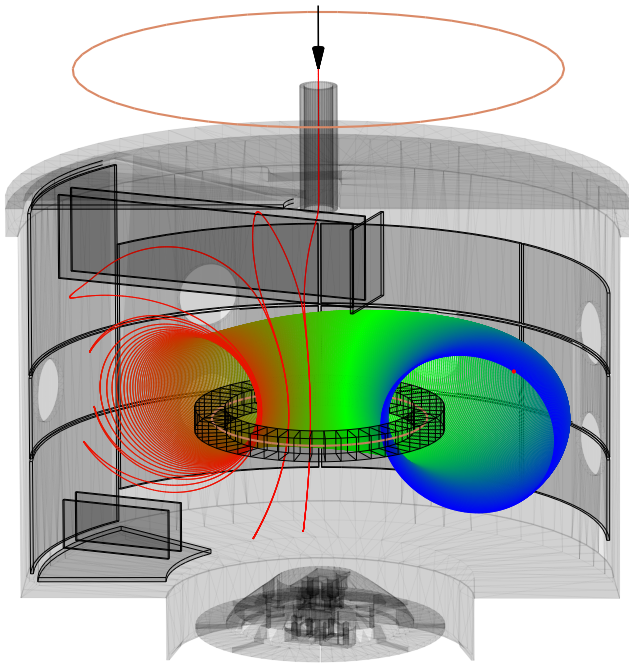


FIG. 12. Simulation of injection of a positron into APEX-LD. The particle is represented by the red dot (right), and the color gradient (red-green-blue line) represents the passage of time along its trajectory. It enters from above along the cylindrical axis and passes through the $E \times B$ plates, undergoing several poloidal reflections between the biased lifter/wall electrodes before drifting onto a closed field line. The injected positron drifts toroidally in the clockwise direction (viewed from above).

strated experimentally.^{54,56}

APEX-LD has also been designed with diagnostics for pair plasmas in mind. The primary diagnostic for annihilation gamma-rays is an array of 48 bismuth germanate (BGO) detectors (not shown in Fig. 1). The detector arrangement will exploit the open geometry of the LD to maximize the coverage of lines of response for coincidence detection of back-to-back 511 keV gamma rays.⁵⁷ Additional planned diagnostics include capacitive wall probes mounted inside the heat shield, and a pulsed gas jet to instigate annihilation events.

ACKNOWLEDGMENTS

The authors would like to thank J. Horn-Stanja, H. Saitoh, and T. Sunn Pedersen for their contributions to the project, as well as THEVA GmbH for collaboration on the coil designs. We also acknowledge the guidance of C. Hugenschmidt and R. Neu, and support from the DFG (HU 978/20-1, STE 2614/2-1), ERC (Horizon 2020, Grant 741322), NSF (PHY-2206620), DOE (DE-SC0016532), the UCSD Foundation, and the Helmholtz Association (VH-NG-1430).

....

¹V. Tsytovich and C. B. Wharton, Comments Plasma Phys. Controlled Fusion **4**, 91 (1978).

²P. Helander, Physical Review Letters **113**, 135003 (2014).

³W. Horton, Reviews of Modern Physics **71**, 735 (1999).

⁴T. Siebert, R. Diehl, J. Greiner, M. G. H. Krause, A. M. Beloborodov, M. C. Bel, F. Guglielmetti, J. Rodriguez, A. W. Strong, and X. Zhang, Nature **531**, 341 (2016).

⁵T. Siebert, Astrophysics and Space Science **368**, 27 (2023).

⁶Y. Chen, R. Ding, Y. Liu, Y. Mizuno, J. Shu, H. Yu, and Y. Zeng, Physical Review Letters **135**, 121001 (2025), publisher: American Physical Society.

⁷C. D. Arrowsmith, P. Simon, P. J. Bilbao, A. F. A. Bott, S. Burger, H. Chen, F. D. Cruz, T. Davenne, I. Efthymiopoulos, D. H. Froula, A. Goillot, J. T. Gudmundsson, D. Haberberger, J. W. D. Halliday, T. Hodge, B. T. Huffman, S. Iaquina, F. Miniati, B. Reville, S. Sarkar, A. A. Schekochihin, L. O. Silva, R. Simpson, V. Stergiou, R. M. G. M. Trines, T. Vieu, N. Charitonidis, R. Bingham, and G. Gregori, Nature Communications **15**, 5029 (2024).

⁸G. Sarri, K. Poder, J. M. Cole, W. Schumaker, A. Di Piazza, B. Reville, T. Dzelzainis, D. Doria, L. A. Gizzi, G. Grittani, S. Kar, C. H. Keitel, K. Krushelnick, S. Kuschel, S. P. D. Mangles, Z. Najmudin, N. Shukla, L. O. Silva, D. Symes, A. G. R. Thomas, M. Vargas, J. Vieira, and M. Zepf, Nature Communications **6**, 6747 (2015).

⁹T. S. Pedersen, J. R. Danielson, C. Hugenschmidt, G. Marx, X. Sarasola, F. Schauer, L. Schweikhard, C. M. Surko, and E. Winkler, New Journal of Physics **14**, 035010 (2012).

¹⁰M. R. Stoneking, T. S. Pedersen, P. Helander, H. Chen, U. Hergenhan, E. V. Stenson, G. Fiksel, J. von der Linden, H. Saitoh, C. M. Surko, J. R. Danielson, C. Hugenschmidt, J. Horn-Stanja, A. Mishchenko, D. Kennedy, A. Deller, A. Card, S. Nißl, M. Singer, M. Singer, S. König, L. Willingale, J. Peebles, M. R. Edwards, and K. Chin, Journal of Plasma Physics **86**, 155860601 (2020).

¹¹J. Danielson, D. Dubin, R. Greaves, and C. Surko, Reviews of Modern Physics **87**, 247 (2015).

¹²C. Hugenschmidt, C. Piochacz, M. Reiner, and K. Schreckenbach, New Journal of Physics **14**, 055027 (2012), publisher: IOP Publishing.

¹³M. Dickmann, W. Egger, G. Kögel, S. Vohburger, and C. Hugenschmidt, Acta Physica Polonica A **137**, 149 (2020).

¹⁴E. V. Stenson, J. Horn-Stanja, M. R. Stoneking, and T. S. Pedersen, Journal of Plasma Physics **83**, 595830106 (2017).

¹⁵S. Earnshaw, Trans. Cambridge Philos. Soc. **7**, 97 (1842).

¹⁶S. Yoshikawa, Nuclear Fusion **13**, 433 (1973).

¹⁷S. M. Krimigis, T. P. Armstrong, W. I. Axford, C. O. Bostrom, C. Y. Fan, G. Gloeckler, L. J. Lanzerotti, E. P. Keath, R. D. Zwicky, J. F. Carbarry, and D. C. Hamilton, AAAS New Series **206**, 977 (1979).

¹⁸A. Hasegawa, Comments on Plasma Physics and Controlled Fusion **11**, 147 (1987).

¹⁹A. Hasegawa, L. Chen, and M. Mauel, Nuclear Fusion **30**, 2405 (1990).

²⁰D. Garnier, A. Hansen, J. Kesner, M. Mauel, P. Michael, J. Minervini, A. Radovinsky, A. Zhukovsky, A. Boxer, J. Ellsworth, I. Karim, and E. Ortiz, Fusion Engineering and Design **81**, 2371 (2006).

²¹T. Mito, N. Yanagi, Y. Hishinuma, Y. Ogawa, J. Morikawa, K. Ohkuni, M. Iwakuma, T. Uede, S. Nose, I. Itoh, and S. Fukui, IEEE Transactions on Applied Superconductivity **13**, 1500 (2003).

²²Y. Ogawa, Z. Yoshida, J. Morikawa, H. Saito, S. Watanabe, Y. Yano, S. Mizumaki, and T. Tosaka, Plasma and Fusion Research **4**, 020 (2009).

²³A. C. Boxer, D. T. Garnier, J. L. Ellsworth, J. Kesner, and M. E. Mauel, Journal of Fusion Energy **27**, 11 (2008).

²⁴M. Nishiura, Z. Yoshida, H. Saitoh, Y. Yano, Y. Kawazura, T. Nogami, M. Yamasaki, T. Mushiake, and A. Kashyap, Nuclear Fusion **55**, 053019 (2015), publisher: IOP Publishing.

²⁵Z. Yoshida, H. Saitoh, J. Morikawa, Y. Yano, S. Watanabe, and Y. Ogawa, Physical Review Letters **104**, 235004 (2010), publisher: American Physical Society.

²⁶J. File, G. D. Martin, R. G. Mills, and K. E. Wakefield, Journal of Applied Physics **42**, 6 (1971).

²⁷A. Zhukovsky, M. Morgan, D. Garnier, A. Radovinsky, B. Smith, J. Schultz, L. Myatt, S. Pourrahimi, and J. Minervini, IEEE Transactions on Applied Superconductivity **10**, 1522 (2000).

²⁸B. Smith, J. Schultz, A. Zhukovsky, A. Radovinsky, C. Gung, P. Michael, J. Minervini, J. Kesner, D. Garnier, M. Mauel, G. Naumovich, and R. Kocher, IEEE Transactions on Applied Superconductivity **11**, 2010 (2001).

²⁹Y. Ogawa, J. Morikawa, T. Mito, N. Yanagi, and M. Iwakuma, Fusion Engineering and Design **81**, 2361 (2006).

- ³⁰S. Mizumaki, T. Tosaka, Y. Ohtani, M. Ono, T. Kuriyama, K. Nakamoto, M. Shibui, N. Tachikawa, S. Ioka, J. Morikawa, Y. Ogawa, and Z. Yoshida, IEEE Transactions on Applied Superconductivity **16**, 918 (2006).
- ³¹N. Yanagi, T. Mito, Y. Hishinuma, Y. Ogawa, J. Morikawa, K. Ohkuni, M. Iwakuma, T. Uede, S. Nose, and I. Itoh, IEEE Transactions on Applied Superconductivity **13**, 1504 (2003).
- ³²T. Tosaka, Y. Ohtani, M. Ono, T. Kuriyama, S. Mizumaki, M. Shibui, K. Nakamoto, N. Tachikawa, J. Morikawa, Y. Ogawa, and Z. Yoshida, IEEE Transactions on Applied Superconductivity **16**, 910 (2006).
- ³³A. Zhukovsky, J. Schultz, B. Smith, A. Radovinsky, D. Garnier, O. Filatov, V. Beljakov, S. Egorov, V. Kuchinsky, A. Malkov, E. Bondarchouk, V. Korsunsky, and V. Sytnikov, IEEE Transactions on Applied Superconductivity **11**, 1873 (2001).
- ³⁴C. S. Chisholm, T. Berry, D. T. Garnier, R. A. Badcock, G. Bioletti, K. Bouloukakos, E.-K. Brewerton, M. A. Buchanan, P. J. Burt, E. V. W. Chambers, K. B. Chappell, P. Coulson, R. J. Davidson, J. P. M. Ellingham, P. Geursen, K. Hamilton, R. Hu, E. Hunter, J. P. Jones, P. Kusay, Z. Lazić, B. Leuw, M. Lynch, R. Mataira, M. McCrohon, L. Meadows, J. R. Morris, R. Nowacki, J. V. Purvis, J. H. P. Rice, M. Rutten, S. Schimanski, A. Sharma, M. Siamaki, A. Simpson, T. Simpson, B. Smith, E. Stiers, E. Swanson-Dobbs, J. Todd, E. O. P. Treacher, J. D. Tyler, S. Venturumilli, H. W. Weijers, T. Wordsworth, and N. Zhou, "Design and initial results from the "Junior" Levitated Dipole Experiment," (2025), arXiv:2508.17691 [physics].
- ³⁵V. S. Foote, IEEE Transactions on Nuclear Science **18**, 85 (1971).
- ³⁶J. Kesner and M. Mauel, "Levitated Dipole Experiment," Tech. Rep. Notice 03-19 (U.S. Department of Energy, 2003).
- ³⁷J. Morikawa, K. Ohkuni, D. Hori, S. Yamakoshi, T. Goto, Y. Ogawa, N. Yanagi, and T. Mito, TEION KOGAKU (Journal of the Cryogenic Society of Japan) **39**, 209 (2004).
- ³⁸J. Morikawa, Z. Yoshida, Y. Ogawa, S. Watanabe, Y. Yano, S. Mizumaki, T. Tosaka, Y. Ohtani, and M. Shibui, Fusion Engineering and Design **82**, 1437 (2007).
- ³⁹A. Card, *A compact levitated dipole for the confinement of electron-positron pair plasmas*, Ph.D. thesis, Technical University of Munich (2025).
- ⁴⁰A. Card, A. Deller, M. R. Stoneking, J. v. d. Linden, and E. V. Stenson, IEEE Transactions on Applied Superconductivity **34**, 1 (2024).
- ⁴¹Y. Shi, N. H. Babu, K. Iida, and D. A. Cardwell, Journal of Physics: Conference Series **97**, 012250 (2008).
- ⁴²Since the Hastelloy substrate has relatively poor electrical and thermal conductivities, there is a preferred side to the tape for electrical and thermal connections.
- ⁴³H. Saitoh, M. R. Stoneking, and T. S. Pedersen, Review of Scientific Instruments **91**, 043507 (2020).
- ⁴⁴Recently replaced with a Heinzinger Power Converter 50-200.
- ⁴⁵J. C. Simpson, J. E. Lane, C. D. Immer, R. C. Youngquist, and T. Steinrock, Kennedy Space Center **NASA Technical Reports Server** (2001).
- ⁴⁶A. Deller, V. C. Bayer, P. Steinbrunner, A. Card, J. R. Danielson, M. R. Stoneking, and E. V. Stenson, Plasma Physics and Controlled Fusion **67**, 015030 (2024), publisher: IOP Publishing.
- ⁴⁷T. G. Northrop and E. Teller, Physical Review **117**, 215 (1960).
- ⁴⁸K. Singha, L. Lachhvani, S. Pahari, D. Raju, R. Goswami, and P. K. Chattopadhyay, Physics of Plasmas **32**, 092109 (2025).
- ⁴⁹J. S. deGrassie and J. H. Malmberg, The Physics of Fluids **23**, 63 (1980).
- ⁵⁰H. Saitoh, Z. Yoshida, J. Morikawa, Y. Yano, H. Hayashi, T. Mizushima, Y. Kawai, M. Kobayashi, and H. Mikami, Physics of Plasmas **17**, 112111 (2010).
- ⁵¹M. Singer, M. R. Stoneking, E. V. Stenson, S. Nißl, A. Deller, A. Card, J. Horn-Stanja, T. Sunn Pedersen, H. Saitoh, and C. Hugenschmidt, Physics of Plasmas **28**, 062506 (2021).
- ⁵²A. Deller, C. Rogge, S. Desopo, E. Stenson, J. Danielson, M. Stoneking, C. Hugenschmidt, T. Sunn Pedersen, and C. Surko, Journal of Plasma Physics **89**, 935890602 (2023).
- ⁵³M. Singer, J. Danielson, S. König, T. S. Pedersen, L. Schweikhard, and E. Stenson, Journal of Plasma Physics **89**, 935890501 (2023).
- ⁵⁴E. Stenson, S. Nißl, U. Hergenbahn, J. Horn-Stanja, M. Singer, H. Saitoh, T. S. Pedersen, J. Danielson, M. Stoneking, M. Dickmann, and C. Hugenschmidt, Physical Review Letters **121**, 235005 (2018).
- ⁵⁵S. Nißl, E. V. Stenson, U. Hergenbahn, J. Horn-Stanja, T. Sunn Pedersen, H. Saitoh, C. Hugenschmidt, M. Singer, M. R. Stoneking, and J. R. Danielson, Physics of Plasmas **27**, 052107 (2020).
- ⁵⁶A. Deller, J. Von Der Linden, S. Nißl, K. Michishio, N. Oshima, H. Higaki, and E. V. Stenson, Physical Review E **110**, L023201 (2024).
- ⁵⁷J. Von Der Linden, S. Nißl, A. Deller, J. Horn-Stanja, J. Danielson, M. Stoneking, A. Card, T. Sunn Pedersen, and E. Stenson, Journal of Plasma Physics **89**, 905890511 (2023).